Chemical Science

EDGE ARTICLE

View Article Online
View Journal | View Issue

Cite this: *Chem. Sci.*, 2017, **8**, 6619

A thin multifunctional coating on a separator improves the cyclability and safety of lithium sulfur batteries†

Guiyin Xu,[ab] Qing-bo Yan,[bc] Shitong Wang,[b] Akihiro Kushima,[bd] Peng Bai,[ef] Kai Liu,[b] Xiaogang Zhang,*[a] Zilong Tang[g] and Ju Li*[bh]

Received 2nd May 2017
Accepted 9th July 2017

DOI: 10.1039/c7sc01961k

rsc.li/chemical-science

Lithium–sulfur batteries are one of the most promising next-generation batteries due to their high theoretical specific capacity, but are impeded by the low utilization of insulating sulfur, unstable morphology of the lithium metal anode, and transport of soluble polysulfides. Here, by coating a layer of nano titanium dioxide and carbon black onto a commercial polypropylene separator, we demonstrate a new composite separator that can confine the polysulfides on the cathode side, forming a catholyte chamber, and at the same time block the dendritic lithium on the anode side. Lithium–sulfur batteries using this separator show a high initial capacity of 1206 mA h g^{-1} and a low capacity decay rate of 0.1% per cycle at 0.5C. Analyses reveal the electrocatalytic effect and the excellent dendrite-blocking capability of the ~7 μm thick coating.

Introduction

Lithium–sulfur (Li–S) batteries are attractive due to their low cost and high gravimetric energy density,[1–3] but suffer from low cyclability and poor safety in energy-density-optimized full cells due to (a) soluble polysulfide shuttling from the cathode to anode, and (b) lithium metal anode corrosion and shorting.[4,5] In order to defeat (a), there are two strategies (Scheme 1a): (a1) adsorption + electrocatalysis, and (a2) complete sealing by a solid electrolyte. In (a1), the sulfur cathode is mixed with electrocatalyst nanoparticles that compete with the liquid electrolyte for free polysulfides. The electrocatalysts (such as graphene oxide[6,7] and TiO_2 [8–11]) also facilitate the redox reactions of the surface-adsorbed polysulfides. The (a1) route reduces the concentrations and lifetimes of soluble polysulfides, thereby reducing – but not eliminating – sulfur transport to the lithium anode. In the (a2) strategy, one aims to eliminate sulfur crossover completely by sealing off the cathode chamber using a solid electrolyte that conducts Li^+ but not sulfur.[12] This is possible because diffusion mechanisms are fundamentally different in solids ("hopping/exchange") than those in liquids ("vehicular" Stokes–Einstein transport of all soluble species). A solid barrier formed *in situ* with no percolating pores could stop sulfur transport completely while still allowing bidirectional Li^+ transport, forming an enclosed catholyte chamber on the sulfur side. Moreover, a negatively charged Debye layer near the separator surface could reject the polysulfide anions to localize their transport on the cathode side[13] and the functional interlayers could also trap lithium polysulfides.[14,15] In order to defeat (b), in particular electrical shorting by dendritic penetration of the separator,[16] a deformable solid electrolyte separator is also envisioned, which blocks lithium dendrite growth more effectively than traditional nanoporous polypropylene (PP) separators at large current densities.

While lithium metal growth always chases the ionic current and thus the ~30 nm pores in the PP separator, there can be a thermodynamic cost when the pores get very small. Depending on the over-potential applied to the anode, there is a smallest radius-of-curvature for depositing lithium metal allowed by thermodynamics due to capillary forces.[17] While lithium metal dendrite is able to plate through the 30 nm pores of the PP separator, it may find it difficult to plate through the much smaller pores of our coating. *In situ* transmission electron microscopy (TEM) observations of mossy lithium growth reveal

[a]Jiangsu Key Laboratory of Material and Technology for Energy Conversion, College of Material Science and Engineering, Nanjing University of Aeronautics and Astronautics, Nanjing 210016, P. R. China. E-mail: azhangxg@nuaa.edu.cn
[b]Department of Nuclear Science and Engineering, Massachusetts Institute of Technology, Cambridge, Massachusetts 02139, USA. E-mail: liju@mit.edu
[c]College of Materials Science and Opto-Electronic Technology, University of Chinese Academy of Sciences, Beijing 100049, P. R. China
[d]Department of Materials Science and Engineering, Advanced Materials Processing and Analysis Center, University of Central Florida, Orlando, Florida 32826, USA
[e]Department of Chemical Engineering, Massachusetts Institute of Technology, Cambridge, Massachusetts 02139, USA
[f]Department of Energy, Environmental and Chemical Engineering, Washington University in St. Louis, Saint Louis, Missouri 63130, USA
[g]State Key Lab of New Ceramics and Fine Processing, School of Materials Science and Engineering, Tsinghua University, Beijing 100084, P. R. China
[h]Department of Materials Science and Engineering, Massachusetts Institute of Technology, Cambridge, Massachusetts 02139, USA

† Electronic supplementary information (ESI) available: Detailed description of the experimental procedures and calculations. See DOI: 10.1039/c7sc01961k

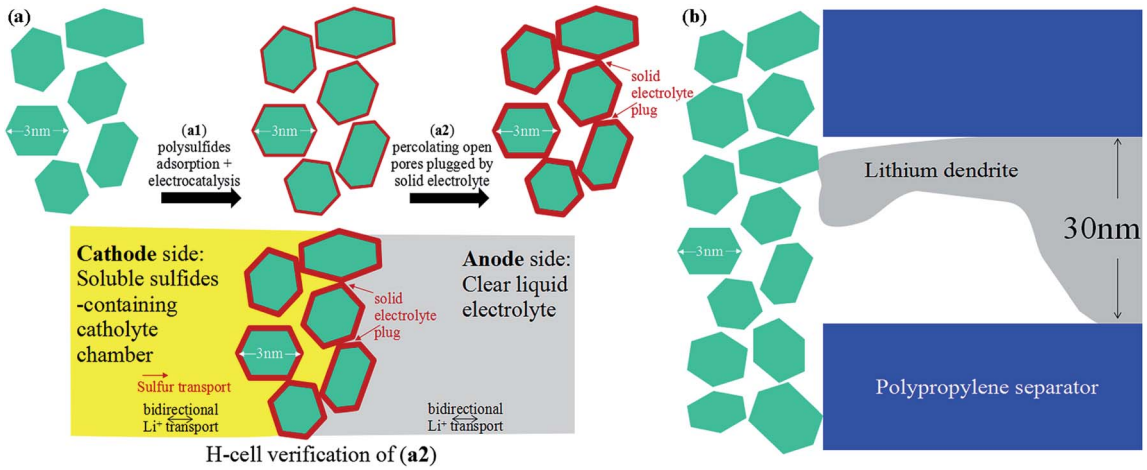

Scheme 1 (a) Illustration of two strategies for counteracting polysulfide shuttling in Li–S batteries. (b) Lithium dendrite may find it difficult to plate through few-nm nanopores.

that even under a very large overpotential,[18] the smallest mossy lithium tendrils have radii of tens of nanometers, so the fine pores of our ceramic coating could present significant resistance to lithium metal dendrite growth (Scheme 1b), while still allowing bidirectional Li^+ transport. When this coating is applied without carbon black (*e.g.* to the opposite side of the PP separator), it could add a significant safety factor against electrical shorting.[19–21]

In this work, we propose a multifunctional coating less than 10 μm thick, easily applied onto traditional nanoporous PP separators, which addresses (a1), (a2) and (b) simultaneously. This porous coating consists of titanium dioxide nanoparticles and carbon black, forming an excellent adsorbent, and is electronically conductive and electrocatalytically active, verified by shifted redox voltage peaks and theoretical calculations (a1). Later, this thin porous coating gets fouled by solid sulfur-containing compounds, forming an *in situ* solid electrolyte layer that stops sulfur transport while still allowing bidirectional Li^+ transport. Ideally, if the sulfur-containing solid electrolyte formed *in situ* closes all percolating pores, we will have (a2). To demonstrate this, we applied the fouled coated separator (after cycling) in a H-cell, and showed it can separate the polysulfide containing left side (dark color) with the clear side, demonstrating that it can be used to form a catholyte chamber. Lastly, for (b), we showed that the sub-10 μm thick coating on 30 μm thick PP can delay dendrite penetration for a 15× longer time duration, at an extremely large current density of 100 mA cm^{-2}, using a capillary tube cell setup for visualization. These findings prove that such a thin nano oxide coating is multifunctional in enhancing the cycle life and safety of Li–S batteries.

Results and discussion

Lithium polysulfides dissolved in the organic electrolyte can easily diffuse through the polypropylene separator and react with the lithium metal anode (Fig. 1a),[22–24] resulting in poor cycling performance.[19,20] Therefore, preventing polysulfide migration by separator modification is a promising strategy to increase the electrochemical performance of Li–S batteries.[25–27] Herein, we prepared titanium dioxide nanoparticles with high Li^+ conductivity and large specific surface area as a coating on separators (Fig. 1b). The size of the titanium dioxide nanoparticles is ~3 nm (Fig. 1c and S1†). The amorphous and nanocrystalline phases of the titanium dioxide nanoparticles are shown in area 1 and area 2 (Fig. 1d), respectively. The amorphous phase of TiO_2 has high lithium ion mobility, which is beneficial for lithium ion diffusion.[28] The lattice fringes with a distance of 0.19 nm correspond to the (200) plane of anatase TiO_2 (Fig. S2 and S3†). Moreover, the titanium dioxide nanoparticles show a relatively high specific surface area of 313 m^2 g^{-1} with a major pore size of 2.5 nm (Fig. S4†), and thus have a large contact area with soluble lithium polysulfides.

The pristine polypropylene separator shows abundant pores on the surface and has a thickness of ~30 μm (Fig. S5†). After

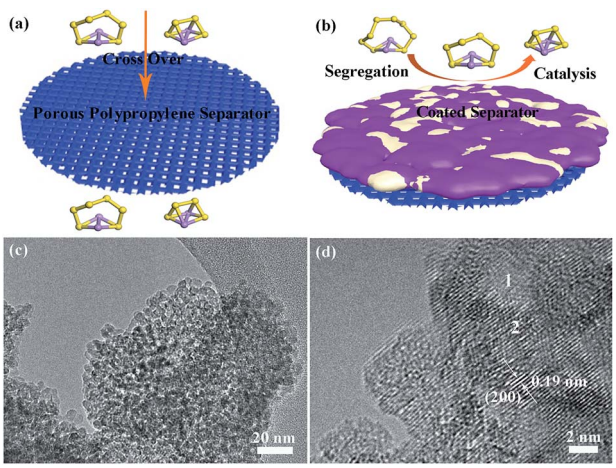

Fig. 1 Schematic illustrations of Li–S batteries with (a) a pure polypropylene and (b) a coated separator. (c) Transmission electron microscopy (TEM) and (d) high-resolution transmission electron microscopy (HRTEM) images of the titanium dioxide nanoparticles.

coating with either solely the super C65 or the mixture of titanium dioxide nanoparticles and super C65, the surfaces of these separators become denser (Fig. 2a and c). The thickness of these coating layers is ~7.5 μm (Fig. 2b and d), and the loadings of the coating material are 0.4 mg cm^{-2} for the C65 separator and 0.7 mg cm^{-2} for the TiO–C65 separator. The coated separator retains its mechanical flexibility, which is important for battery fabrication (Movie S1†). Elemental mapping of the super C65 separator shows that carbon is mainly dispersed on the surface (Fig. S6†). Titanium, oxygen, and carbon are uniformly dispersed on the surface of the TiO–C65 separator (Fig. 2e–h).

To characterize the distribution of sulfur species on the cycled TiO–C65 separator, we performed local probe mechanical tests. In Fig. 2i–l (ESI Movie S2†), we pushed in a sharp tungsten probe from the top of the layer, and then moved it horizontally to execute a scratching test. The particle size on the separator turns out to be bigger compared to that before cycling (Fig. 2c and d), indicating agglomeration bonded by the deposited sulfide (a2 in Scheme 1a). Solid-like sulfur species were confirmed to be deposited on the TiO–C65 coating (Fig. 2i and S12a†). Meanwhile, C65 mixed in the coating (which is in physical contact with the solid cathode) can act as an additional cathode current collector to reuse the lithium polysulfides. When the vertical force applied on the probe is small, we find that there is no extra soft film formed on the surface, unlike in the case of using an acidized carbon nanotube paper on the separator.[12] Thus, the lithium polysulfides should be dispersed inside the ~7.5 μm TiO–C65 coating.

From cyclic voltammetry curves, there are two reduction peaks of the S_8 cathode in Li–S batteries (Fig. 3a).[29–31] The first peak at high voltage corresponds to the open ring reduction of sulfur to soluble lithium polysulfides (Li_2S_n, $4 \leq n \leq 8$) and the second peak is attributed to the transformation of the lithium polysulfides to insoluble Li_2S_2/Li_2S.[32] In our Li–S battery test with the C65 separator, the second reduction peak appears in the 3rd cycle (Fig. S7†). However, the TiO–C65 separator Li–S batteries exhibit the second reduction peak after the 1st cycle, and the peak position and shape remain stable from the 2nd cycle on. The cathodic peak positions of the TiO–C65 separator (2.254 and 1.925 V) are larger than the C65 separator (2.221 and 1.850 V), indicating faster redox reaction kinetics. This demonstrates that titanium dioxide nanoparticles have a strong electrocatalytic effect on sulfur reduction (Fig. 3a). There is a small anodic peak at 1.9 V in Li–S batteries with the TiO–C65 separator, corresponding to the lithiation of TiO_2 (Fig. S8†). Moreover, the overpotential ΔU between the anodic peaks and cathodic peaks of the TiO–C65 separator (0.246 and 0.464 V) is smaller than that of the C65 separator (0.251 and 0.544 V), indicating the lower polarization of Li–S batteries with the TiO–C65 separator.

Li–S batteries with the TiO–C65 coated separator show a high specific capacity of 1601 mA h g^{-1} at a current density of 0.1C (1C ≡ 1675 mA g^{-1}) and a good rate performance at higher current densities (Fig. 3b). Moreover, the two plateaus in the discharged curve were still evident even up to 1C (Fig. S9†). Typically, the low electronic conductivity of sulfur and the high solubility of lithium polysulfides are associated with the low

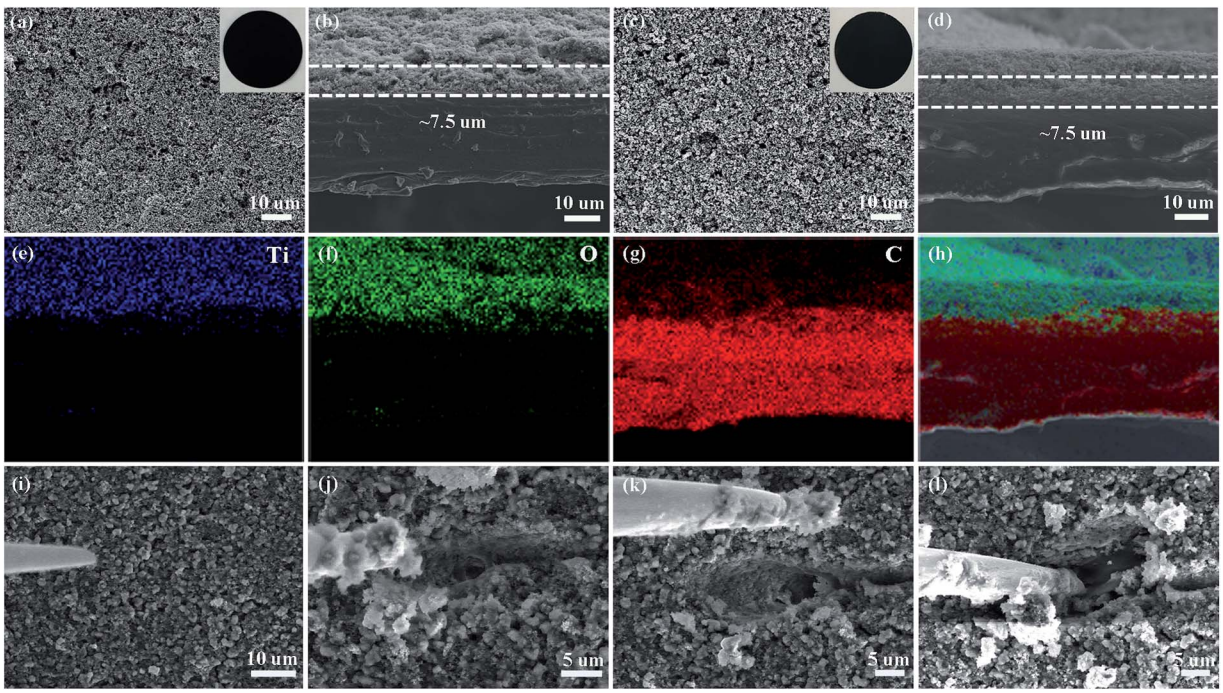

Fig. 2 Scanning electron microscopy (SEM) images of the super C65 (C65) separator (a) surface and (b) cross-section, and the titanium dioxide-super C65 (TiO–C65) separator (c) surface and (d) cross-section. The insets in (a) and (c) are digital photographs of the C65 and TiO–C65 separators. (e–h) Energy-dispersive X-ray spectroscopy (EDS) elemental mapping images for the region shown in (d): titanium, oxygen, and carbon. (i–l) Scratching test of the cycled TiO–C65 separator (see Movie S2†) by a nano-manipulator tip shown in SEM images.

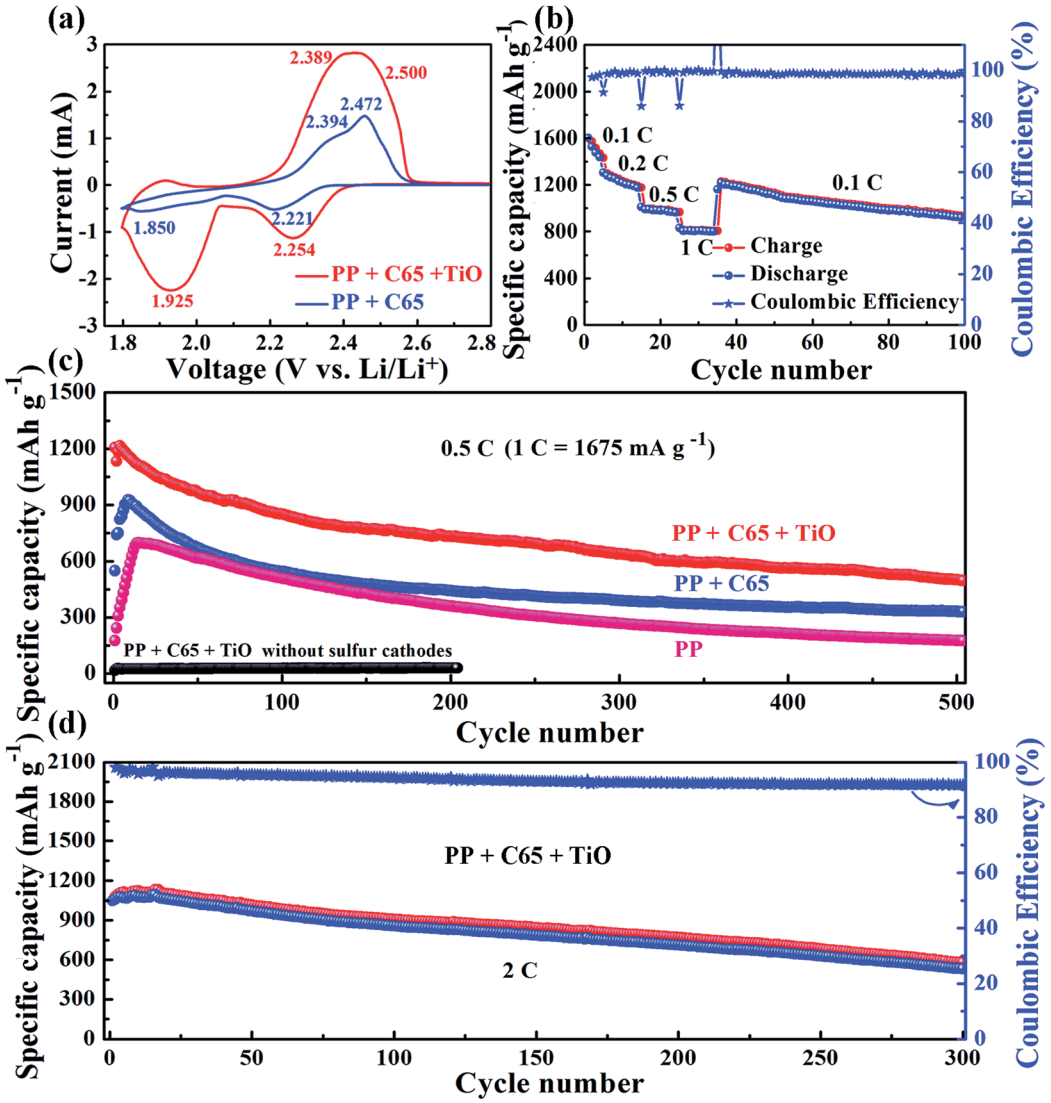

Fig. 3 (a) Typical cyclic voltammetry (CV) curves of the sulfur cathode with the TiO–C65 and C65 separator in the 3rd cycle at a scan rate of 0.2 mV s^{-1}. (b) Rate capability of the sulfur cathode with the TiO–C65 separator. Cycling performance of sulfur cathodes based on the PP, TiO–C65, and C65 separators at a constant rate of (c) 0.5C and (d) 2C.

utilization of sulfur and poor cycling performance of Li–S batteries. In fact, our test with the PP separator shows a low specific capacity of only 175 mA h g^{-1} at a current density of 0.5C (Fig. 3c). On the other hand, the conductive C65 coating on the separator confines the polysulfides within the cathode side, forming a catholyte chamber. Therefore, Li–S batteries with the C65 separator have a higher specific capacity of 550 mA h g^{-1} at the first cycle and maintain a discharged capacity of 332 mA h g^{-1} after 500 cycles at 0.5C. Li–S batteries with the TiO–C65 separator have a high initial capacity of 1206 mA h g^{-1} and a high maintained capacity of 501 mA h g^{-1} after 500 cycles at 0.5C.

The titanium dioxide nanoparticles have a strong catalytic effect and chemical binding with lithium polysulfides, which not only has the potential to increase the utilization but also to improve the rate performance. For example, the charge transfer resistance is clearly reduced (see ESI Fig. S10†). The Li–S batteries with the TiO–C65 coated separator also show a good electrochemical performance at a higher current density of 2C with 1047 mA h g^{-1} at the first cycle and 533 mA h g^{-1} after 300 cycles (Fig. 3d). While the sulfur loading is approximately 2 mg cm^{-2}, Li–S batteries with the TiO–C65 separator have an initial capacity of 840 mA h g^{-1} and a high sustained capacity of 556 mA h g^{-1} after 90 cycles at 0.5C (see ESI Fig. S11†). To confirm the ability of the TiO–C65 separator to trap lithium polysulfides, we disassembled the coin cell after the test and performed SEM analysis and found the coexistance of sulfur and titanium (see ESI Fig. S12†). This demonstrates that titanium dioxide nanoparticles can selectively adsorb the sulfur species as a solid-like fouling product.

The trapped sulfur species in the coating can still contribute to the capacity. We constructed a battery cell using the cycled TiO–C65 separator to conduct a cyclic voltammetry scan, and it showed distinct charge/discharge peaks for sulfur (see ESI

Fig. S13†), indicating that the coating can act as a second current collector and reuse the lithium polysulfides trapped within. Thereafter, the fouled TiO–C65 coating (after cycling) was applied in a separate H-shaped cell (see ESI Fig. S14†), and showed it could separate the polysulfide containing left side (dark color) from the clear side, demonstrating that the sulfur-containing solid electrolyte formed *in situ* on the TiO–C65 separator could be used to form an isolated catholyte chamber.

To investigate the effects of TiO_2 on Li_2S_n transport and transformation, systematic first-principles calculations were conducted for a Li_2S_x–graphite (here representing super C65)/TiO_2 surface system. The optimized lowest-energy geometric structures of Li_2S_n (n = 1, 2, 4, 6 or 8) are shown in Fig. S15,† which are consistent with other reported works.[33,34] The structures of Li_2S and Li_2S_2 are similar, with sulfur atoms bridging two lithium atoms. Li_2S_6 and Li_2S_8 show ring-like structures, which can be regarded as a lithium dimer inserted into the S_6 and S_8 rings. Li_2S_4 has a cage-like structure and is the intermediate structure between the above two structural types.

The optimized geometrical models for Li_2S_n (n = 1, 2, 4, 6, or 8) and S_8 adsorbed on the TiO_2 and graphite surfaces are displayed in Fig. 4 and S16,† and the corresponding binding energies are plotted in Fig. 4j. Obviously, the binding energies for Li_2S_n adsorbed on the TiO_2 surface are much larger than those of Li_2S_n on the graphite surface. The binding energy of S_8 on TiO_2 is 1.35 eV, nearly double that for S_8 on graphite (0.72 eV), indicating that TiO_2 can more effectively attract S_8 molecules. For the graphite and TiO_2 surfaces, the adsorption energies for Li_2S_n are all larger than that for S_8, which may be related to the larger polarity of Li_2S_n compared with S_8. The binding energies for Li_2S_n on graphite are around 1.2 eV except for that for Li_2S_4. As shown in Fig. S16,† for Li_2S and Li_2S_2, both lithium atoms are closer to the graphite surface, indicating that the attraction between lithium atoms and graphite is larger than that between sulfur atoms and graphite. On the other hand, the lithium dimers are nearly vertical to the graphite surface for Li_2S_6 and Li_2S_8. This may be because there is more contact area with graphite when the ring-like Li_2S_6 and Li_2S_8 are parallel to the graphite surface which maximizes the binding energies. For Li_2S_4, the dimer is vertical to the graphite surface. However, it does not have a ring-like structure to maximize the contact area, thus showing a lower binding energy (1.0 eV).

Different from graphite, the binding energies of Li_2S_n on TiO_2 dramatically increase with the decrease of n (n = 1, 2, 4, 6, or 8) or increase of lithium fraction. As shown in Fig. 4a–f, the lithium atoms are bonded with two adjacent oxygen atoms at the TiO_2 surface for all of Li_2S_n (n = 1, 2, 4, 6, or 8). While the distances between the nearest neighbor oxygen atoms are 3.79/3.80 Å, the distances between the lithium atoms in Li_2S_n are 3.55, 3.31, 2.85, 2.75, and 2.77 Å, for n = 1, 2, 4, 6, and 8, respectively. Our calculation shows that the TiO_2 surface attracts Li_2S_n (n = 1, 2, 4, 6, or 8) and S_8 molecules much more

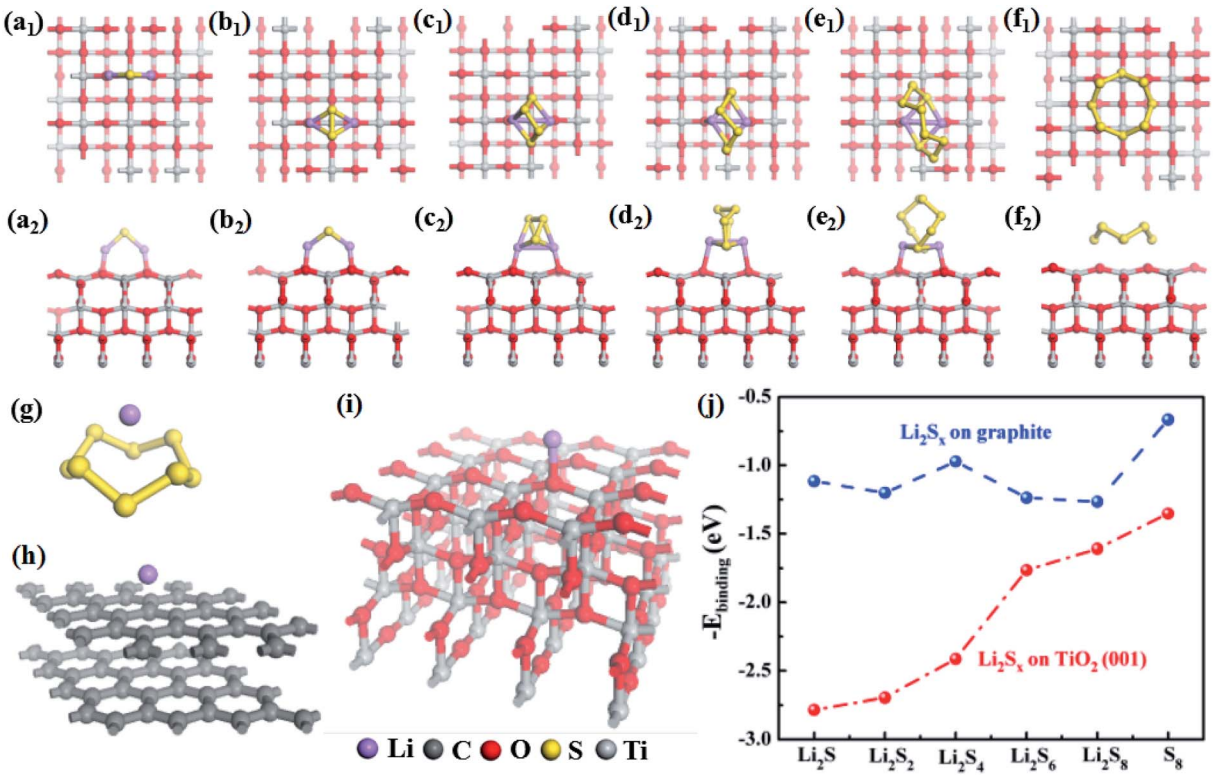

Fig. 4 The optimized geometrical structures of (a–e) Li_2S_n (n = 1, 2, 4, 6, or 8) and (f) S_8 adsorbed on the TiO_2 surface. (a_1–f_1) The upper and (a_2–f_2) lower panels are top and front views of the optimized geometrical structures. The optimized geometrical structures of Li atoms adsorbed on (g) S_8, (h) graphite, and (i) TiO_2. The corresponding binding energies are 2.16, 1.68 and 4.45 eV, respectively. (j) The binding energies for Li_2S_n (n = 1, 2, 4, 6, or 8) and S_8 adsorbed on the surface of graphite and TiO_2.

strongly than graphite. With its large surface area, the nano-size TiO_2 should efficiently adsorb Li_2S_n and reduce the shuttling, substantially enhancing the utilization of lithium and sulfur. This explains the expansion of the peak area in the cyclic voltammetry curves (Fig. 3a) and the dramatic improvement of the capacity at higher rates.

Additionally, we compared the abilities of S_8, graphite and TiO_2 to attract lithium atoms. The calculated binding energies are 2.16, 1.68 and 4.45 eV, for S_8, graphite, and TiO_2, respectively (Fig. 4g, h and i). In the discharge process, lithium ions transport through the separator to react with sulfur atoms. These results give insights into the role of the coating materials on the separator. For example, if there is only carbon (graphite) and no TiO_2 in the separator, the lithium atoms prefer to adsorb on sulfur but not on graphite, because the binding energy of lithium on the former is larger than that on the latter. Therefore, the effect of carbon alone is expected to be small. Moreover, the obtained lowest-energy Li–S_8 adsorption configuration has the lithium atom located above the center of the S_8 molecule (Fig. 4g), and it requires breaking the S_8 ring (overcoming an energy barrier of about 1.5 eV)[35] to form the most stable Li_2S_8 structure (Fig. S15e†). In contrast, the binding energy for the lithium atom on TiO_2 is about twice as large as that on S_8, which allows TiO_2 to attract lithium atoms in addition to S_8 molecules (as discussed above). This leads to the aggregation of lithium atoms and S_8 molecules on the TiO_2 surface. Additionally, each lithium atom releases about 4 eV when binding with TiO_2, which can help the nearby S_8 to overcome the barrier to open the ring and form the Li_2S_8 structure. TiO_2 thus provides an effective electrocatalytic surface by stabilizing the reaction intermediates, and enhancing the rate of reaction between them. Furthermore, it is known that once the size of TiO_2 is smaller than 10 nm, it can become electrically conductive.[36] This electrocatalytic effect for the Li_2S_n transformations explains the peak shifts in the cyclic voltammetry curves (Fig. 3a) and the reduction of the activation period (Fig. 3c).

With the above electrochemical tests and theoretical calculations, we confirm that our TiO–C65 coated membrane can trap lithium polysulfides to improve the performance of Li–S batteries. The nanoparticle coating may exhibit an additional benefit, which is to prevent lithium dendrite penetration. To test the capability of the coated separator to block dendritic lithium penetration, we devised a capillary cell to visualize the electrodeposition process. The capillary cell is filled with the liquid electrolyte, where a piece of lithium metal electrode is stripped and the lithium ions are simultaneously electrodeposited onto an enamelled copper wire with the end wrapped by the separators. The detail of the experimental setup is shown in the ESI Fig. S17.† The diameter of the copper wire is 0.04 cm. The capillary tube batteries are discharged at a high current density of 100 mA cm^{-2} to promote the dendritic growth of lithium metal. Lithium dendrites begin to emerge from the polypropylene separator at 50 s (ESI Movie S3†), while no lithium penetration was observed in the cell using our TiO–C65 separator even after 850 s (ESI Movie S4†). The results indicate that the TiO–C65 coating can act as a multifunctional barrier to prevent the lithium dendrites from penetrating the separator, as well as preventing the cross-over of lithium polysulfides.

Conclusions

In summary, we have developed a multi-functional titanium dioxide–super C65 modified separator for Li–S batteries that enables a high specific capacity, stable cycling performance at high rates, and improved safety. Li–S batteries with the TiO–C65 separator show a high initial capacity of 1206 mA h g^{-1} and maintain a high specific capacity of 501 mA h g^{-1} after 500 cycles at 0.5C. The electrochemical results and theoretical simulation demonstrate that titanium dioxide nanoparticles have a strong catalytic effect and chemical binding with lithium polysulfides. Therefore, the effect of the TiO–C65 separator is assigned to (a1) surface segregation and catalysis, and also the partial effect of (a2) sealing by the solid electrolyte formed *in situ*. The results of this work indicate that thin coating materials with high conductivity and a large surface area on the separator can increase the utilization of lithium polysulfides, allow the fast diffusion of lithium ions, and decrease the migration of lithium polysulfides to the lithium metal anode. Additionally, our titanium dioxide nanoparticle–super C65 separator with a strong dendrite blocking ability can be used in applications beyond Li–S batteries such as lithium/sodium metal batteries, and contributes to the development of high-performance and safe energy storage devices.

Acknowledgements

This work is supported by the National Key Basic Research Program 973 (2014CB239701), National Natural Science Foundation of China (51372116), and Natural Science Foundation of Jiangsu Province (BK20151468). G. X. would like to thank Jiangsu Innovation Program for Graduate Education (KYLX15_0300) for funding. J. L. acknowledges the support of NSF ECCS-1610806.

Notes and references

1 X. Ji, K. T. Lee and L. F. Nazar, *Nat. Mater.*, 2009, **8**, 500–506.
2 Y. Sun, N. Liu and Y. Cui, *Nat. Energy*, 2016, **1**, 16071.
3 Z. Sun, J. Zhang, L. Yin, G. Hu, R. Fang, H. M. Cheng and F. Li, *Nat. Commun.*, 2017, **8**, 14627.
4 C. Huang, J. Xiao, Y. Shao, J. Zheng, W. D. Bennett, D. Lu, L. V. Saraf, M. Engelhard, L. Ji, J. Zhang, X. Li, G. L. Graff and J. Liu, *Nat. Commun.*, 2014, **5**, 3015.
5 J. Lu, Z. Chen, Z. Ma, F. Pan, L. A. Curtiss and K. Amine, *Nat. Nanotechnol.*, 2016, **11**, 1031–1038.
6 L. Ji, M. Rao, H. Zheng, L. Zhang, Y. Li, W. Duan, J. Guo, E. J. Cairns and Y. Zhang, *J. Am. Chem. Soc.*, 2011, **133**, 18522–18525.
7 G. Xu, Q. B. Yan, A. Kushima, X. Zhang, J. Pan and J. Li, *Nano Energy*, 2017, **31**, 568–574.
8 Z. Wei Seh, W. Li, J. J. Cha, G. Zheng, Y. Yang, M. T. McDowell, P. C. Hsu and Y. Cui, *Nat. Commun.*, 2013, **4**, 1331.

9 S. Evers, T. Yim and L. F. Nazar, *J. Phys. Chem. C*, 2012, **116**, 19653–19658.
10 J. Y. Hwang, H. M. Kim, S. K. Lee, J. H. Lee, A. Abouimrane, M. A. Khaleel, I. Belharouak, A. Manthiram and Y. K. Sun, *Adv. Energy Mater.*, 2016, **6**, 1501480.
11 M. Yu, J. Ma, H. Song, A. Wang, F. Tian, Y. Wang, H. Qiu and R. Wang, *Energy Environ. Sci.*, 2016, **9**, 1495–1503.
12 G. Xu, A. Kushima, J. Yuan, H. Dou, W. Xue, X. Zhang, X. Yan and J. Li, *Ad hoc solid electrolyte on acidized carbon nanotube paper improves cycle life of lithium–sulfur batteries*, 2017, to be published.
13 L. Ma, P. Nath, Z. Tu, M. Tikekar and L. A. Archer, *Chem. Mater.*, 2016, **28**, 5147–5154.
14 Z. Xiao, Z. Yang, L. Wang, H. Nie, M. E. Zhong, Q. Lai, X. Xu, L. Zhang and S. Huang, *Adv. Mater.*, 2015, **27**, 2891–2898.
15 G. Liang, J. Wu, X. Qin, M. Liu, Q. Li, Y. B. He, J. K. Kim, B. Li and F. Kang, *ACS Appl. Mater. Interfaces*, 2016, **8**, 23105–23113.
16 K. Liu, P. Bai, M. Z. Bazant, C. A. Wang and J. Li, *J. Mater. Chem. A*, 2017, **5**, 4300–4307.
17 A. Jana, D. R. Ely and R. E. García, *J. Power Sources*, 2015, **275**, 912–921.
18 A. Kushima, K. P. So, C. Su, P. Bai, N. Kuriyama, T. Maebashi, Y. Fujiwara, M. Z. Bazant and J. Li, *Nano Energy*, 2017, **32**, 271–279.
19 L. Li, Y. Chen, X. Guo and B. Zhong, *Polym. Chem.*, 2015, **6**, 1619–1626.
20 N. Deng, W. Kang, Y. Liu, J. Ju, D. Wu, L. Li, B. S. Hassan and B. Cheng, *J. Power Sources*, 2016, **331**, 132–155.
21 Y. Zhu, Y. Yang, L. Fu and Y. Wu, *Electrochim. Acta*, 2017, **224**, 405–411.
22 M. Q. Zhao, Q. Zhang, J. Q. Huang, G. L. Tian, J. Q. Nie, H. J. Peng and F. Wei, *Nat. Commun.*, 2014, **5**, 3410.
23 G. Xu, J. Yuan, X. Tao, B. Ding, H. Dou, X. Yan, Y. Xiao and X. Zhang, *Nano Res.*, 2015, **8**, 3066–3074.
24 Z. Wang, Y. Dong, H. Li, Z. Zhao, H. Bin Wu, C. Hao, S. Liu, J. Qiu and X. W. Lou, *Nat. Commun.*, 2014, **5**, 5002.
25 H. Yao, K. Yan, W. Li, G. Zheng, D. Kong, Z. W. Seh, V. K. Narasimhan, Z. Liang and Y. Cui, *Energy Environ. Sci.*, 2014, **7**, 3381–3390.
26 M. S. Kim, L. Ma, S. Choudhury and L. A. Archer, *Adv. Mater. Interfaces*, 2016, **3**, 1600450.
27 M. S. Kim, L. Ma, S. Choudhury, S. S. Moganty, S. Wei and L. A. Archer, *J. Mater. Chem. A*, 2016, **4**, 14709–14719.
28 R. Xu, J. Li, Z. Tang and Z. Zhang, *Electrochim. Acta*, 2011, **56**, 6330–6335.
29 L. Ma, K. E. Hendrickson, S. Wei and L. A. Archer, *Nano Today*, 2015, **10**, 315–338.
30 G. Xu, P. Nie, H. Dou, B. Ding, L. Li and X. Zhang, *Mater. Today*, 2017, **20**, 191–209.
31 W. Xue, Q. B. Yan, G. Xu, L. Suo, Y. Chen, C. Wang, C. A. Wang and J. Li, *Nano Energy*, 2017, **38**, 12–18.
32 G. Xu, J. Yuan, X. Geng, H. Dou, L. Chen, X. Yan and H. Zhu, *Chem. Eng. J.*, 2017, **322**, 454–462.
33 Q. Zhang, Y. Wang, Z. W. Seh, Z. Fu, R. Zhang and Y. Cui, *Nano Lett.*, 2015, **15**, 3780–3786.
34 J. J. Chen, R. M. Yuan, J. M. Feng, Q. Zhang, J. X. Huang, G. Fu, M. S. Zheng, B. Ren and Q. F. Dong, *Chem. Mater.*, 2015, **27**, 2048–2055.
35 P. Ballone and R. O. Jones, *J. Chem. Phys.*, 2003, **119**, 8704–8715.
36 M. L. Sushko, K. M. Rosso and J. Liu, *J. Phys. Chem. Lett.*, 2010, **1**, 1967–1972.

Supporting Information

Thin Multifunctional Coating on Separator Improves Cyclability and Safety of Lithium Sulfur Battery

Guiyin Xu,[a,b] Qing-bo Yan,[b,c] Shitong Wang,[b] Akihiro Kushima,[b] Peng Bai,[d] Kai Liu,[b]

Xiaogang Zhang,[a,] Zilong Tang,[e] Ju Li[b,f,]**

[a] Jiangsu Key Laboratory of Material and Technology for Energy Conversion, College of Material Science and Engineering, Nanjing University of Aeronautics and Astronautics, Nanjing 210016, China

[b] Department of Nuclear Science and Engineering, Massachusetts Institute of Technology, Cambridge, Massachusetts 02139, USA

[c] College of Materials Science and Opto-Electronic Technology, University of Chinese Academy of Sciences, Beijing 100049, China

[d] Department of Chemical Engineering, Massachusetts Institute of Technology, Cambridge, Massachusetts 02139, USA

[e] State Key Lab of New Ceramics and Fine Processing, School of Materials Science and Engineering, Tsinghua University, Beijing 100084, PR China

[f] Department of Materials Science and Engineering, Massachusetts Institute of Technology, Cambridge, Massachusetts 02139, USA

Experimental Section

Preparation of Titanium Dioxide Nanoparticles. Titanium dioxide nanoparticles were synthesized *via* a simple hydrolysis process of $TiOSO_4 \cdot 2H_2O$ aqueous solutions. The typical procedure was as follows: 0.25 M $TiOSO_4 \cdot 2H_2O$ aqueous solutions were prepared and placed in a 100 mL Teflon-lined autoclave. Then it was heated to 150 °C for 5-120 min. After the hydrothermal reaction, the products were washed by distilled water thoroughly, followed by heat treatment in vacuum to obtain white titanium dioxide powder.

Preparation of the C65 Separator and the TiO-C65 Separator. The 70 wt% titanium dioxide nanoparticles, 20 wt% timcal super C65, and 10 wt% polyvinylidene fluoride (PVDF) were stirred for 12 h in N-methyl pyrrolidinone (NMP) and then were coated on the polypropylene separator by the doctor blade. The separator was dried at 60 °C overnight and the TiO-C65 separator was obtained after the material was cooled to room temperature. The C65 separator consisted of 90 wt% timcal super C65 and 10 wt% PVDF on the polypropylene separator. The other procedures are similar with the TiO-C65 separator.

Characterization. X-ray diffraction (XRD) patterns were measured on a Bruker-AXS D8 DISCOVER. Copper Kα line was used as a radiation source with λ=0.15406 nm. Field emission scanning electron microscopy (FESEM) and transmission electron microscopy (TEM) measurements were carried out with JEOL JSM-6380LV FE-SEM and FEI TECNAI-20, respectively. Scanning transmission electronic microscope (STEM) was performed on a Tecnai G2 F30. The X-ray photoelectron spectroscopy (XPS) analysis was performed on a Perkin-Elmer PHI 550 spectrometer with Al Kα (1486.6 eV) as the X-ray source. The N_2 adsorption/desorption tests were determined by Brunauer-Emmett-Teller (BET) measurements using an ASAP-2010 surface area analyzer. The pore size distribution (PSD) was derived from the desorption branch of the isotherm with the Barrett-Joyner-Halenda (BJH) method.

Electrochemical Characterization. Electrochemical characterization was carried out by galvanostatic cycling in CR2032-type coin cells. The working electrodes were prepared by a slurry coating procedure. The slurry consisted of 60 wt% commercial sulfur, 30 wt% timcal super C65 and 10 wt% polyvinylidene fluoride (PVDF) dissolved in N-methyl pyrrolidinone (NMP), and was uniformly spread on an aluminium foil current collector. Finally, the electrode was dried at 60 °C for 24 h. Each current collector contained *ca* 2.0 mg cm^{-2} material (with *ca* 1.2 mg cm^{-2} S). Test cells were assembled in an argon-filled glove box using the lithium metal anode and the polypropylene separator or the TiO-C65 separator or the C65 separator. The electrolyte was 1 mol L^{-1} LiTFSI and 0.2 mol L^{-1} $LiNO_3$ in a mixed solvent of 1, 3-dioxolane (DOL) and 1, 2-dimethoxyethane (DME) with a volume ratio of 1:1. The amount of the electrolyte used in the cell is ~10 uL. The coin cells were galvanostatically charged-discharged at different current densities between 1.8 and 2.8 V (*vs.* Li/Li^+) using a CR2032 coin cell test instrument (LAND Electronic Co.). The cyclic

voltammetry (CV) measurement was conducted with a Gamry electrochemical workstation at a scan rate of 0.2 mV s^{-1} in the voltage range of 1.8 to 2.8 V (*vs.* Li/Li^+). Electrochemical impedance spectroscopy (EIS) was measured in the frequency range of 100 kHz-10 mHz with an amplitude of 5 mV.

Computational Section. The calculations were performed using Vienna ab initio simulation package (VASP),[1] which was based on density functional theory (DFT)[2] and the projected augmented wave (PAW) method.[3] Generalized gradient approximation (GGA) in the form of Perdew-Burke-Ernzerhof (PBE)[4] was chosen as exchange correlation potential. The DFT-TS method[5] was adopted to take into account the van der Waals interactions. The kinetic energy cutoff for plane wave functions was set to 500 eV. All structures were fully optimized and the maximum force on each atom was less than 0.01 eV $Å^{-1}$. Supercells containing four atomic layers (the bottom bilayer was fixed during optimization) and a vacuum spacing larger than 15 Å was used to model the graphite and TiO_2 (001) surface. Various initial adsorption configurations were considered, and the most stable optimized configurations were used to discuss the binding between Li_2S_n and graphite or TiO_2 surface. The binding energies (E_b) are defined as the difference between the total energy (E_{tot}) of Li_2S_n-surface adsorption systems, and the energy sum of Li_2S_x and graphite or TiO_2 surface:

$$E_b = (E_{Li_2S_n} + E_{surface}) - E_{tot}$$

Under the above definition, the calculated positive or negative binding energies represent attraction and repel interactions between Li_2S_n and graphite or TiO_2 surface, respectively. The more positive binding energy corresponds to the stronger adsorption.

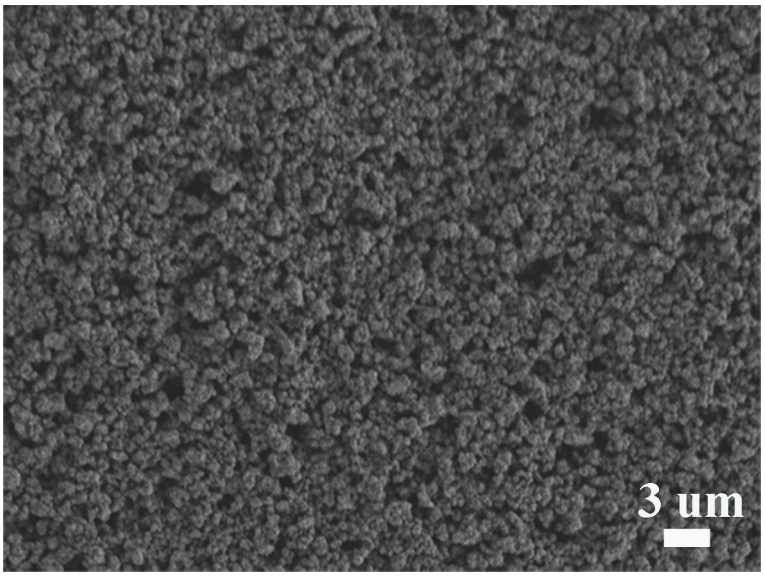

Figure S1. Scanning electron microscopy (SEM) image of titanium dioxide nanoparticles.

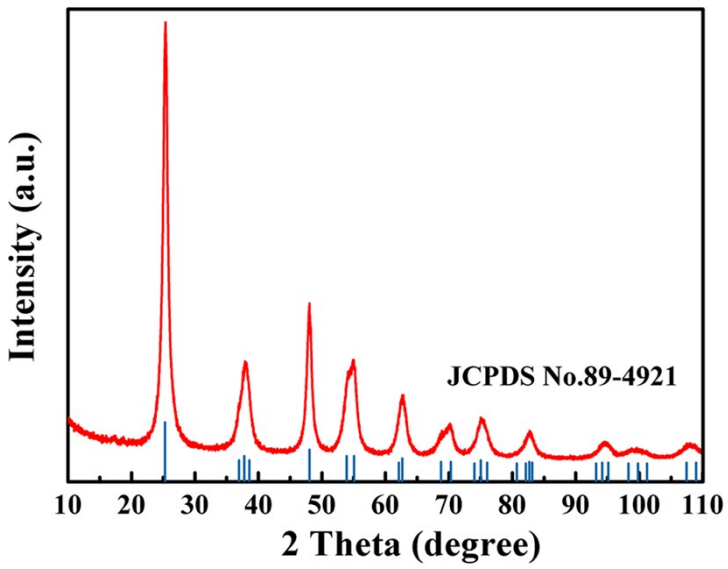

Figure S2. XRD pattern of titanium dioxide nanoparticles.

The XRD pattern of the as-prepared sample shows the diffraction peaks consistent with anatase TiO_2 (JCPDS No. 89-4921) with the planes indexed. The very weak intensity suggests a poorly crystallized structure and possible containing of amorphous phase.

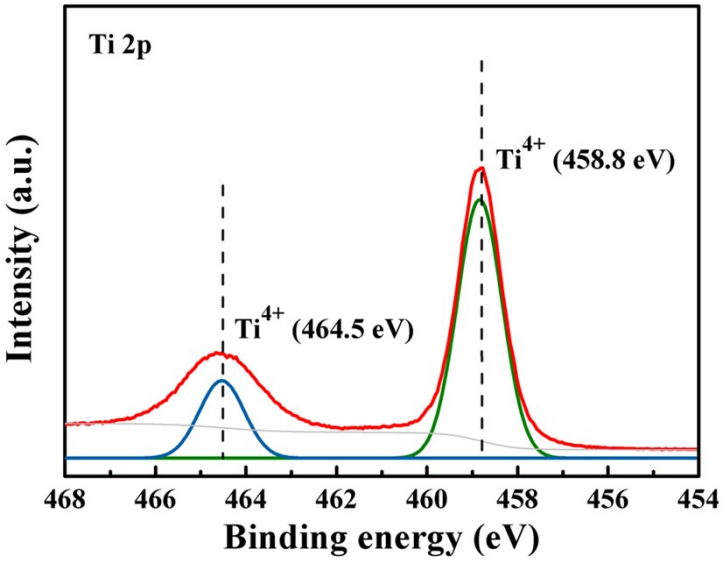

Figure S3. Ti 2*p* XPS spectra of titanium dioxide nanoparticles (Red: observed data; Gray: background; Blue and green: fitting data).

Ti 2*p* X-ray photoelectron spectroscopy (XPS) spectra shows similar features of Ti^{4+} ions due to the Ti $2p_{3/2}$ (≈458.8 eV), Ti $2p_{1/2}$ (≈464.5 eV),[6] and no Ti^{3+} signal is detected.[7-9]

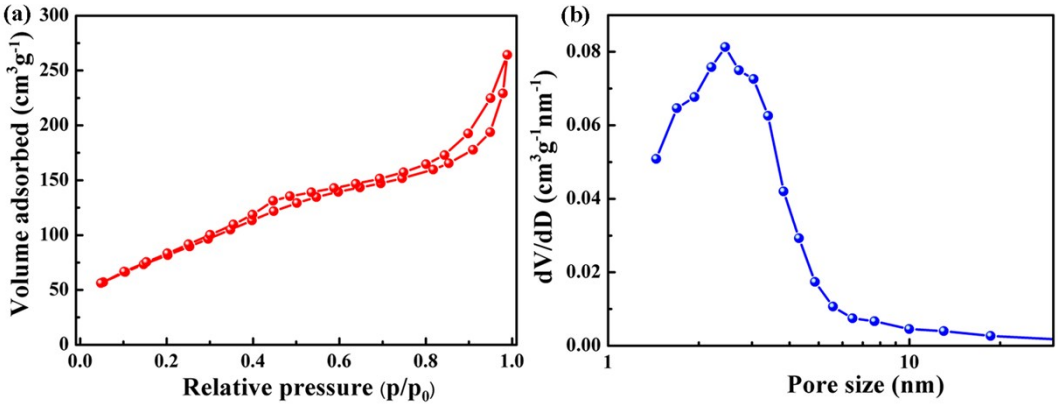

Figure S4. (a) N_2 adsorption/desorption isotherms at 77 K and (b) pore size distribution (PSD) curves of titanium dioxide nanoparticles. PSD is calculated using the Barrett-Joyner-Halenda (BJH) method.

Titanium dioxide nanoparticles show a relatively high surface area of 313 m^2 g^{-1} with a major pore size of 2.5 nm.

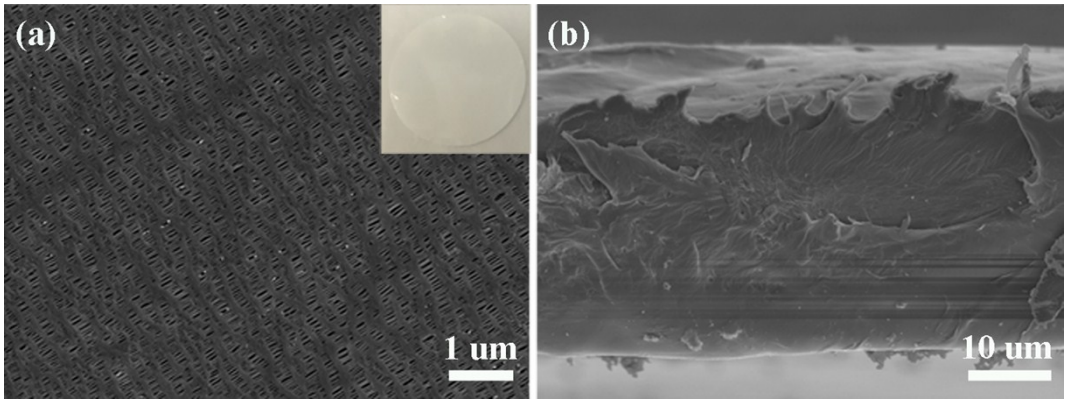

Figure S5. SEM images of the polypropylene (PP) separator (a) surface and (b) cross-section. The inset in **Figure S5a** is the digital photograph of the PP separator.

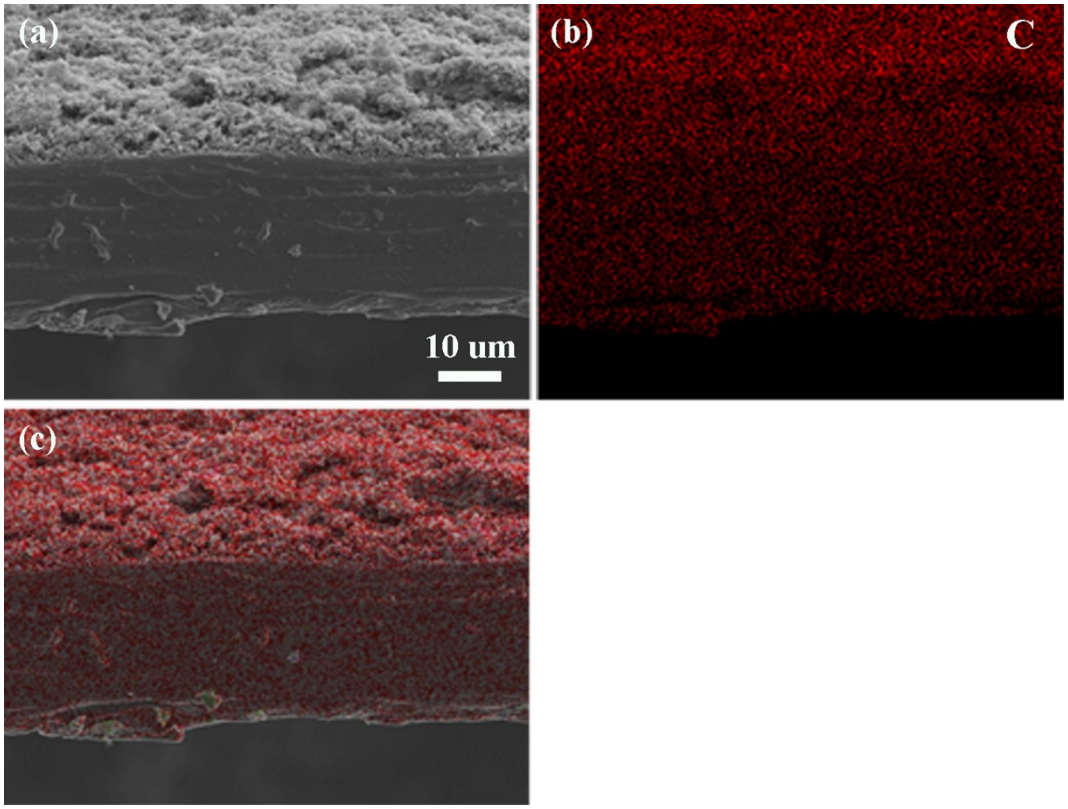

Figure S6. (a) SEM image of the C65 separator and (b) corresponding elemental mapping image of carbon.

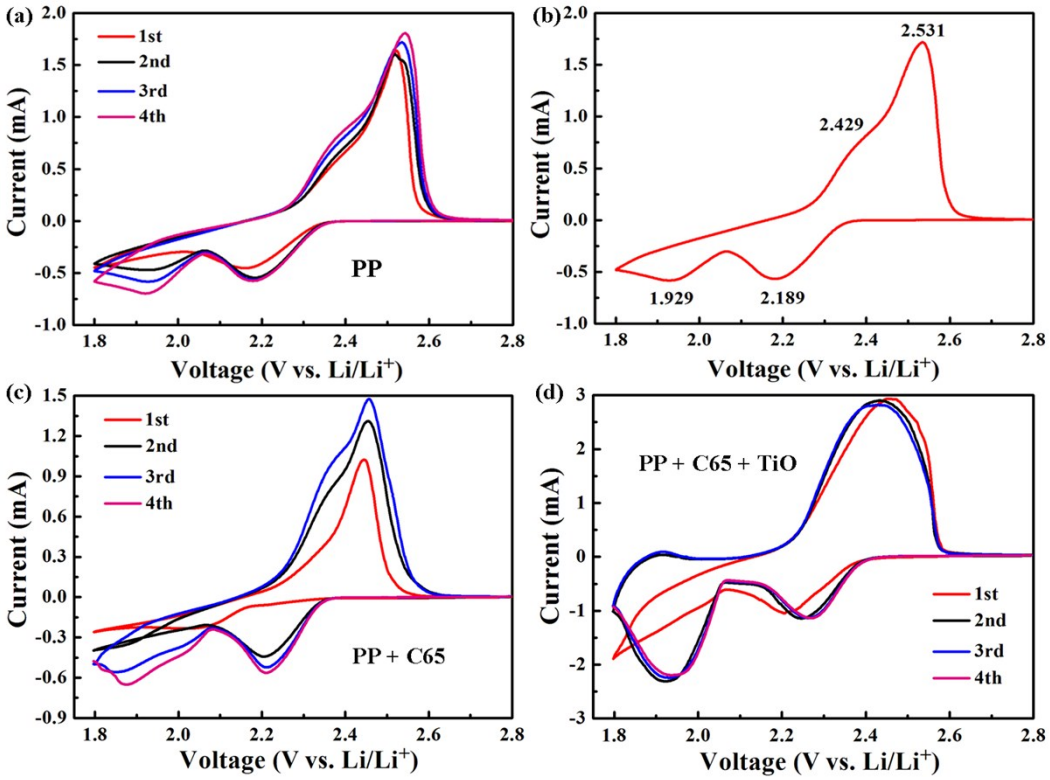

Figure S7. Typical cyclic voltammetry (CV) curves of the sulfur cathode with (a, b) the PP separator, (c) the C65 and (d) TiO-C65 coated separator before cycling at a scan rate of 0.2 mV s^{-1}. (b) CV curve of the sulfur cathode with the PP separator in the 3rd cycle. The cathodic peak position of the PP separator (2.189 V) is smaller than that of the TiO-C65 separator (2.254 V) and the C65 separator (2.221 V). Moreover, the overpotential ΔU between the anodic peak and cathodic peak of the PP separator (0.342 V) is larger than that of the TiO-C65 separator (0.246 V) and the C65 separator (0.251 V).

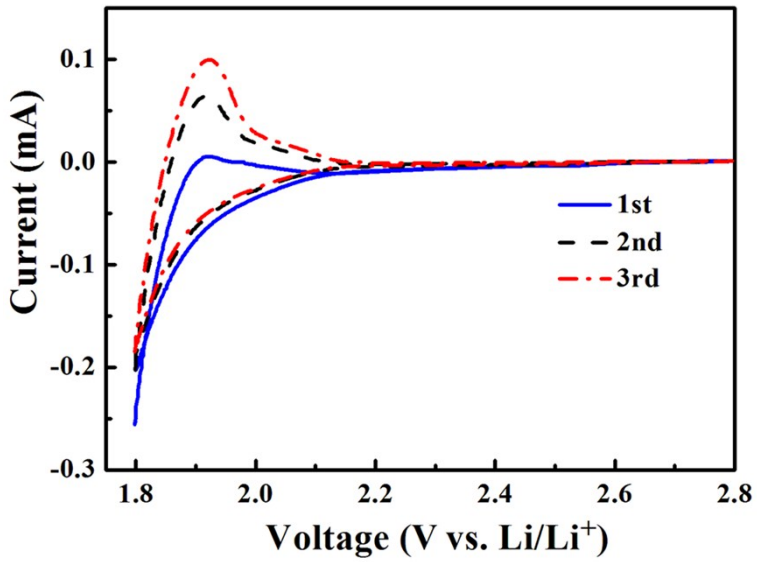

Figure S8. Typical cyclic voltammetry (CV) curves of the TiO-C65 coated separator without sulfur cathode before cycling at a scan rate of 0.2 mV s^{-1}.

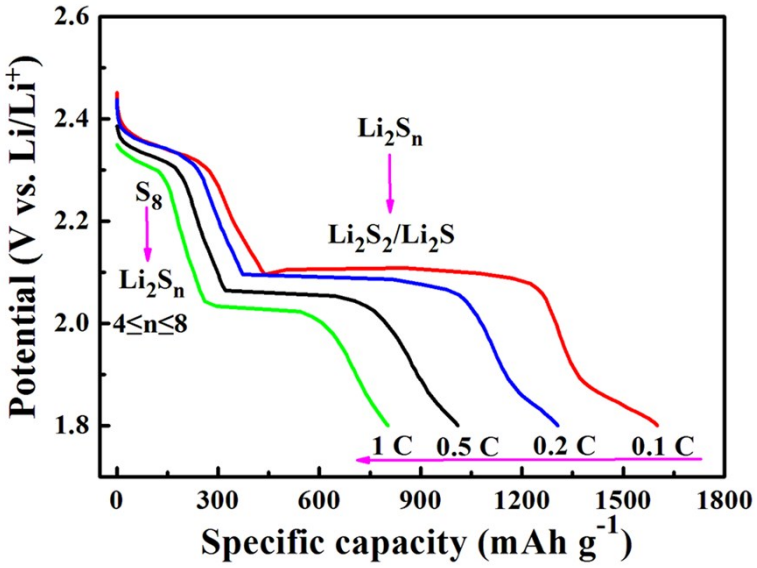

Figure S9. Galvanostatic discharge profiles at different rates of the sulfur cathode with the TiO-C65 coated separator.

The two plateaus correspond to the reduction peaks in **Figure 3a**. The first plateau in high potential corresponds to the open ring reduction of S_8 to soluble lithium polysulfides (Li_2S_n, $4 \leq n \leq 8$) and the second plateau is attributed to the transformation of the lithium polysulfides to insoluble Li_2S_2/Li_2S.

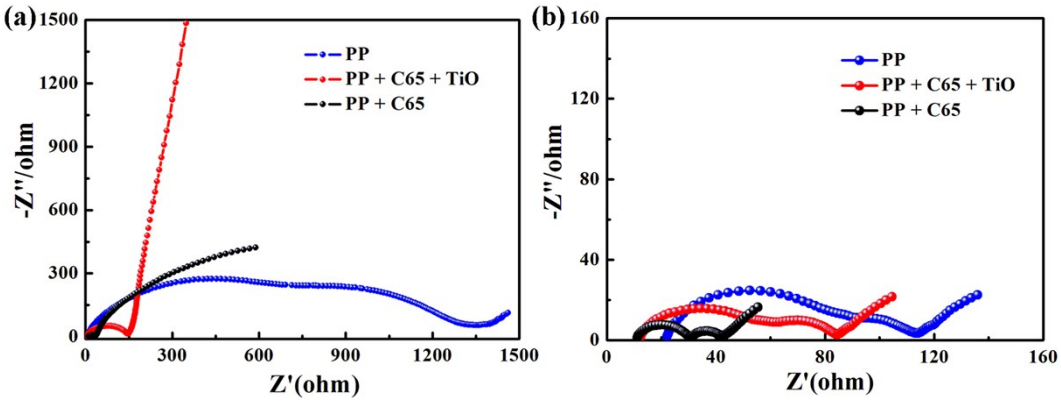

Figure S10. Impedance plots of sulfur cathodes based on the PP separator, TiO-C65 coated separator, and C65 coated separator (a) before cycling and (b) after 100 cycles at at a current density of 0.5 C.

The impedance plots consist of a straight line in the low frequency region corresponding to the ion diffusion (the Warburg impedance, W) and a semicircle in the high frequency region relating to the interface charge-transfer process (the charge transfer resistance, R_{ct}) before cycling.[10] The charge transfer resistance of the TiO-C65 separator and C65 separator is smaller than that of the PP separator (**Figure S10a**). For the sulfur cathodes after 100 cycles at a current density of 0.5 C, the impedance plots exhibit two depressed semicircles and a sloping line (**Figure S10b**). The charge transfer resistance of the TiO-C65 separator and C65 separator is also smaller than that of the PP separator.

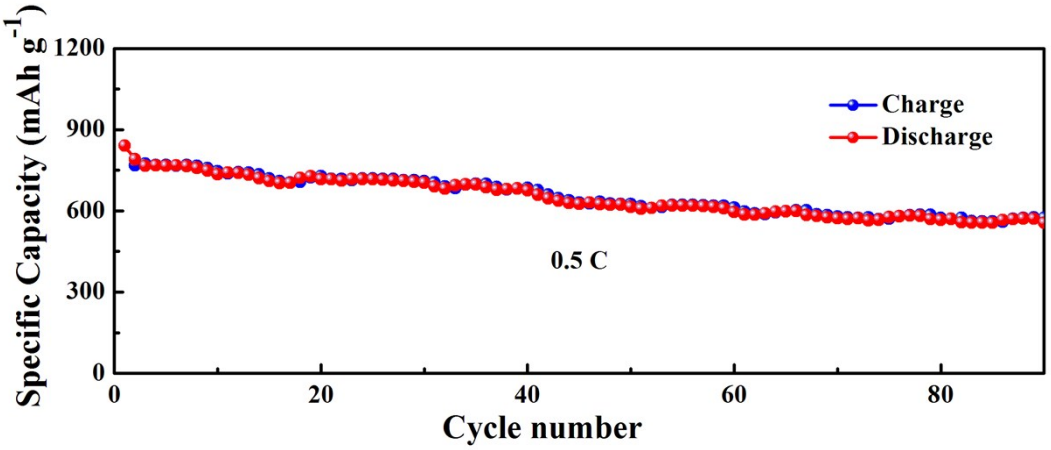

Figure S11. Cycling performance of the sulfur cathode based on the TiO-C65 separator at a current density of 0.5 C. The sulfur loading is *ca* 2 mg cm^{-2}.

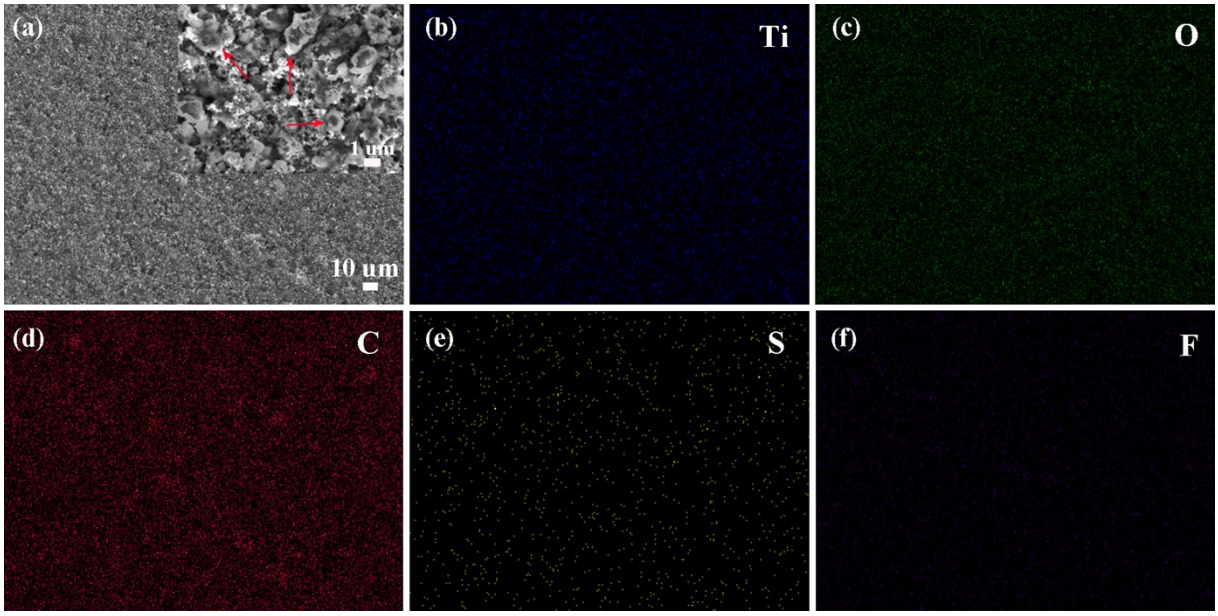

Figure S12. SEM and energy-dispersive X-ray spectroscopy (EDS) characterization of the TiO-C65 coated separator after 50 cycles at 0.5 C (charged state): (a) SEM images of the cycled TiO-C65 separator. The sulfur active material deposition is shown in the red arrow. (b-f) EDS elemental maps for the region shown in (a): (b) titanium, (c) oxygen, (d) carbon, (e) sulfur, and (f) fluorine.

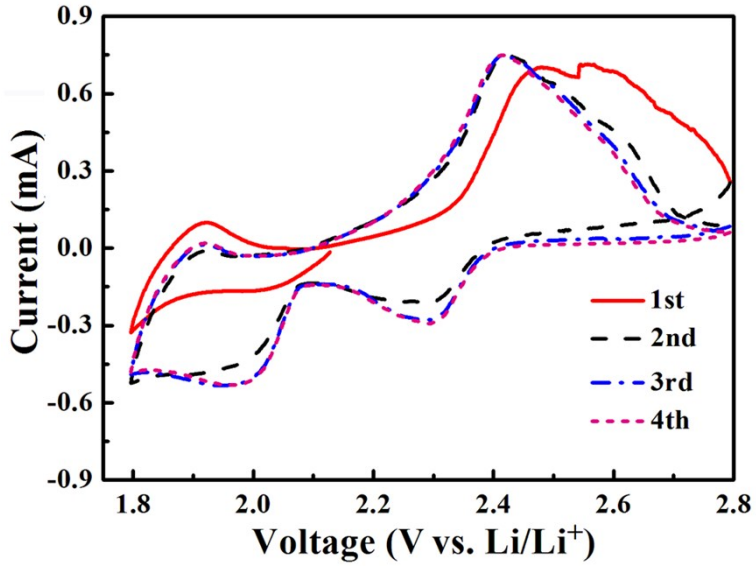

Figure S13. Typical CV curves of the cycled TiO-C65 separator (after 50 cycles at 0.5 C) without sulfur cathode at a scan rate of 0.2 mV s^{-1}.

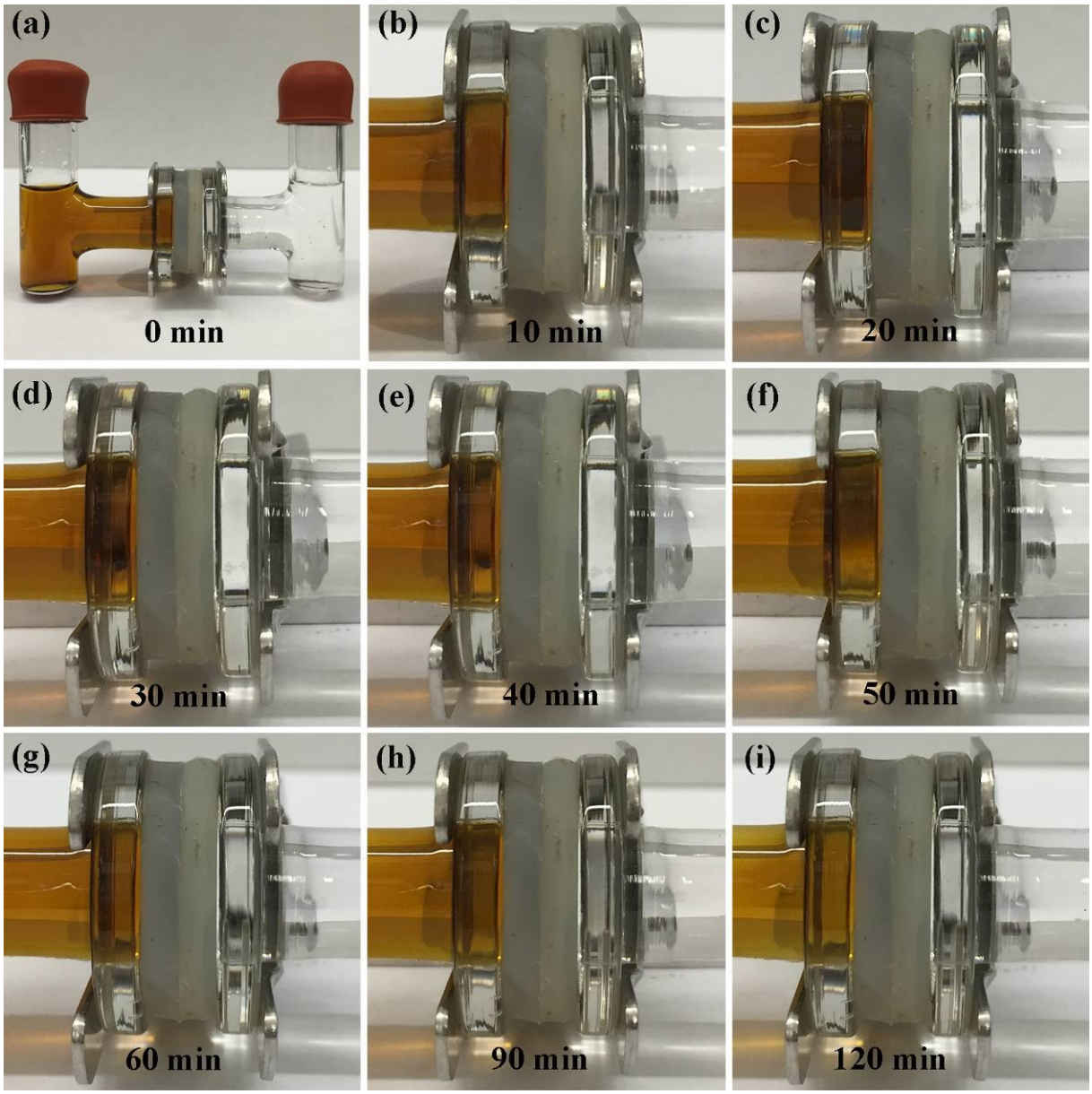

Figure S14. Digital photographs of the H-cell with the cycled TiO-C65 separator at different times.

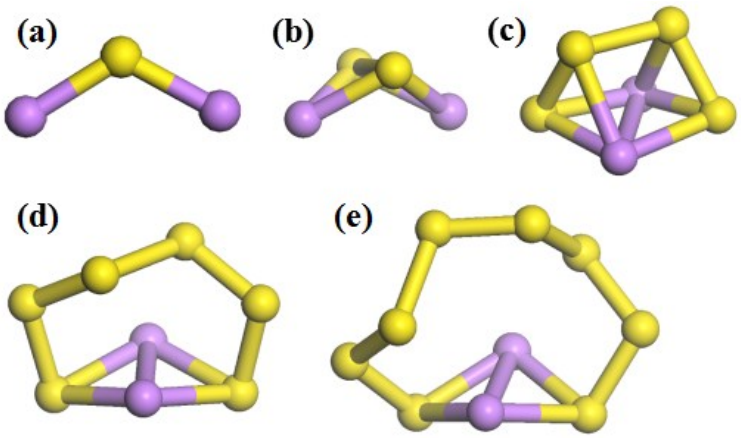

Figure S15. The optimized geometrical structures of Li_2S_n (n=1, 2, 4, 6, 8). Yellow is sulfur atom while purple is lithium atom.

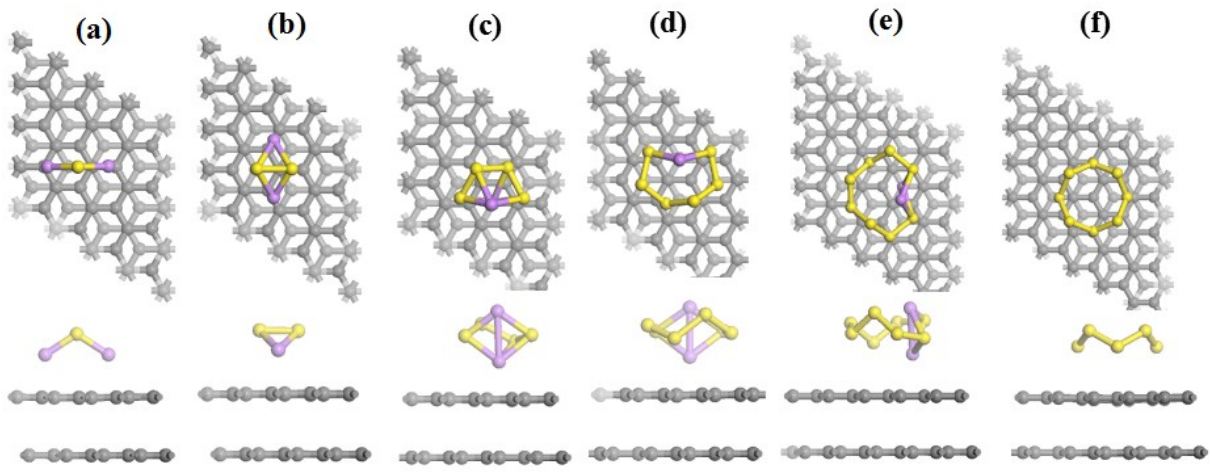

Figure S16. The optimized geometrical structures of (a-e) Li_2S_n (n=1, 2, 4, 6, 8) and (f) S_8 adsorbed on graphite. The upper and lower panels are top and front views, respectively. Only the top two layers of graphite are shown here.

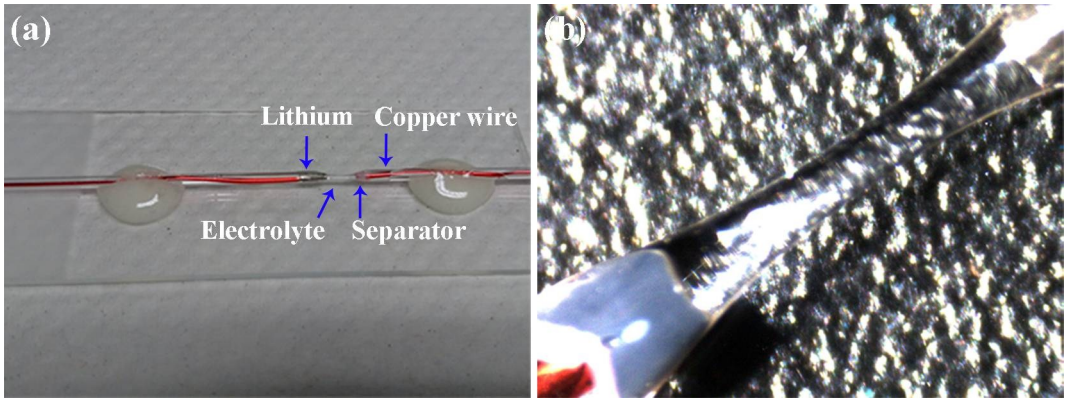

Figure S17. (a) Digital photographs of the capillary tube battery and (b) local enlarged image in the center of a.

Movie S1. The appearance and flexibility of the TiO-C65 separator.

Movie S2. The tension of the cycled TiO-C65 separator after 50 cycles at 0.5 C (Played at x5 original speed).

Movie S3. The capillary tube battery based on the polypropylene separator (Played at x5 original speed).

Movie S4. The capillary tube battery based on the TiO-C65 separator (Played at x5 original speed).

References

1 G. Kresse and J. Furthmüller, *Phys. Rev. B*, 1996, **54**, 11169-11186.

2 P. Hohenberg and W. Kohn, *Phys. Rev.*, 1964, **136**, B864-B871.

3 G. Kresse and D. Joubert, *Phys. Rev. B*, 1999, **59**, 1758-1775.

4 J. P. Perdew, K. Burke and M. Ernzerhof, *Phys. Rev. Lett.*, 1996, **77**, 3865-3868.

5 A. Tkatchenko and M. Scheffler, *Phys. Rev. Lett.*, 2009, **102**, 073005.

6 J. Chen, W. Song, H. Hou, Y. Zhang, M. Jing, X. Jia and X. Ji, *Adv. Funct. Mater.*, 2015, **25**, 6793-6801.

7 L. Shen, E. Uchaker, X. Zhang and G. Cao, *Adv. Mater.,* 2012, **24**, 6502-6506.

8 A. Naldoni, M. Allieta, S. Santangelo, M. Marelli, F. Fabbri, S. Cappelli, C. L. Bianchi, R. Psaro and V. Dal Santo, *J. Am. Chem. Soc.* 2012, **134**, 7600-7603.

9 X. Chen, L. Liu, P. Y. Yu and S. S. Mao, *Science* 2011, **331**, 746-750.

10 G. Xu, J. Han, B. Ding, P. Nie, J. Pan, H. Dou, H. Li and X. Zhang, *Green Chem.* 2015, **17**, 1668-1674.